

1 Behaviour and constitutive modelling of ductile damage of Ti-6Al-
2 1.5Cr-2.5Mo-0.5Fe-0.3Si alloy under hot tensile deformation

3 Junling Li^a, Baoyu Wang^{a,*}, He Huang^a, Shuang Fang^b, Ping Chen^a, Jie Zhao^c, Yi
4 Qin^c

5 ^a *School of Mechanical Engineering, University of Science and Technology Beijing,
6 Beijing 100083, China*

7 ^b *Beijing Institute of Aeronautical Materials, Beijing 100095, China*

8 ^c *Centre for Precision Manufacturing, DMEM, The University of Strathclyde, Glasgow,
9 UK*

10 *Corresponding author: Baoyu Wang

11 E-mail address: bywang@ustb.edu.cn (Baoyu Wang), jlli@xs.ustb.edu.cn (Junling Li)

12 Tel.: +86 10 82375671

13 Fax.: +86 10 62332923

14 Postal address: No.30 Xueyuan Road, Haidian District, Beijing 100083, China

15 **Abstract** In this paper, the flow softening and ductile damage of TC6 alloy were
16 investigated using a uniaxial hot tensile test with deformation temperatures of
17 910 °C~970 °C and strain rates of 0.01 s⁻¹~10 s⁻¹. Scanning electron microscopy (SEM)
18 was performed on the deformed specimens to reveal the damage mechanism. The
19 results showed that the flow stress rapidly increases to a peak at a tiny strain, followed
20 by a significant decrease due to flow softening and ductile damage. The ductile damage
21 of the studied TC6 alloy can be ascribe to the nucleation, growth and coalescence of
22 microdefects, and the microvoids preferentially nucleate at the interface of the alpha
23 phase and beta matrix due to the inconsistent strain. Then, a set of unified viscoplastic
24 constitutive equations including flow softening and ductile damage mechanisms was
25 developed and determined, and this set of equations was verified by the experimental
26 flow stress, which indicated the reliability of the prediction. Furthermore, the predicted
27 normalized dislocation density and the adiabatic temperature rise increase with
28 decreasing temperature and increasing strain rate. The predicted damage components
29 show that the microdefects mainly nucleate in the initial stage, but then primarily grow

30 and link together with continuing deformation.

31 **Keywords:** ductile damage, flow behaviour, titanium alloy, unified constitutive
32 model, micro defects, nucleation

33 1 Introduction

34 Titanium and its alloys have been widely used in aircraft and automotive engines
35 due to their superior specific strength, high operating temperature and corrosion
36 resistance. Plastic forming processes, such as forging, hot stamping and extrusion, are
37 the dominant and effective technologies used to manufacture titanium alloy
38 components^[1]. However, the microstructure and mechanical properties of titanium
39 alloys are very sensitive to the deformation parameters during the high-temperature
40 plastic forming, and combined with their lower thermal conductivity and larger
41 deformation heating, the forming window of titanium alloys has been limited^[2, 3].
42 Consequently, the principal considerations of relevant research are the influence of
43 deformation parameters on the flow behaviour and microstructure evolution. A number
44 of works on the flow behavior and microstructure evolution associated with constitutive
45 modelling have been performed^[3-8]. Bai et al.^[9] proposed a set of unified elastic-
46 viscoplastic constitutive equations based on mechanisms to model the flow softening
47 of Ti-6Al-4V alloy. The mechanisms of globularisation induced by beta strain,
48 dislocation evolution, and adiabatic heating were considered. Huang et al.^[10]
49 characterized the dynamic recrystallization (DRX), flow instability and texture of
50 compressed Ti-6.5Al-3.5Mo-1.5Zr-0.3Si alloy with an equiaxed microstructure. They
51 found that the DRX decreases the fraction of low angle boundaries (LABs) and
52 increases the fraction of high angle boundaries (HABs). Luo et al.^[11] investigated the
53 effects of processing parameters on the flow stress, the strain rate sensitivity and the
54 strain hardening exponent of TC18 alloy. The results showed that thermal and
55 microstructure-related softening are competing with the work hardening to control flow
56 behaviour. Gao et al.^[12] studied the flow behaviour and microstructure evolution of
57 TA15 alloy with a nonuniform microstructure consisting of equaxed and lamellar α
58 phase. The results showed that the lamellar α phase undertakes most of the deformation
59 and turns to be bended and globularized, inducing the higher softening rate than
60 equaxed α phase.

61 Ductile fracture is another increasingly important issue during the high-
62 temperature plastic forming of titanium alloy. The most important area in which our
63 knowledge of ductile fracture is the macroscopic consequence of the nucleation, growth
64 and coalescence of the micro defects, such as voids and cracks^[13-16]. Semiatin et al.^{[17,}
65 ^[18]investigated the cavitation during hot tension testing of Ti-6Al-4V alloy with several
66 different types of transformed beta phase, and the results showed that the cavity
67 initiation occurred due to an obvious mismatch deformation. Dong et al.^[19] investigated
68 the cavity nucleation of Ti-6Al-2Zr-1Mo-1V alloy with the colony alpha microstructure
69 using the isothermal hot compression test. The results showed that most of the cavities
70 nucleated along the prior beta phase boundaries, and the increase of the volume fraction
71 of the beta phase helps to inhibit cavity nucleation. Nicolaou et al. ^[20] proposed that the

cavity initiation sites are different within notch of different sizes, due to the difference in local stress states, and the cavity growth rate was also correlated to the stress state. The effect of the strain rate and stress triaxiality on the tensile behaviour of Ti-10V-2Fe-3Al alloy at were also investigated by Bobbili et al. [21].

One of the most difficult tasks encountered in well documenting the damage behaviour and underlying mechanism is to develop dependable models for accurately simulation and predication. Historically, Cockcroft and Latham developed an empirical damage criterion based on the energy accumulation theory (C-L model), which recognizes that the fracture occurs once when the maximum tensile stress reaches a threshold^[22]. Then, this criterion was modified by Brozzo et al.^[23], in which the hydrostatic pressure was introduced. Likewise, Johnson-Cook (J-C model)^[24], McClintock^[25], Oyane^[26] and Rice and Tracey^[27] successively proposed damage criteria. These phenomenological damage models have been increasingly applied to fracture prediction in the bulk forming due to their easy implementation in the commercial finite element (FE) software as well as the parameter identification. A further framework for damage prediction is the porosity model, whose foundation is based on the micromechanics concepts. The Gurson model, proposed by Gurson^[28], is a typical representation, in which a plastic potential equation to describe the effect of the damage holes was developed. However, the hole size and the spacing between the holes were not taken into account. Therefore, Tvergaard and Needleman et al.^[29, 30] improved the predictive accuracy by substituting the porosity with a variable, and the improved models came to be known of as GTN models.

The aforementioned damage models have been widely used due to their simplicity. However, the simplicity brings about the shortcomings. The big issue is the uncoupling of damage and plasticity, which means that the effect of damage cannot be transiently and continuously fed back to the plastic deformation. Therefore, the continuum damage mechanics (CDM) have received ever-increasing attention. Much research has been carried out to develop the CDM models and understand microscopic fracture behaviour. Hayhurst et al.^[31] investigated the creep fracture of a welding part at high temperature, and established the relationship between the damage internal variable and creep strain rate. Lin et al.^[32] developed a set of generalized constitutive equations to reveal the nucleation and growth of the damage. This set of equations has been successfully applied to many types of materials^[33-35]. Huo et al.^[33] developed a multiaxial constitutive model coupling the microstructure and ductile damage of a high-speed railway axle steel during cross wedge rolling, the result showed that the developed model can reliably predict the grain size and ductile damage evolution. Xiao et al.^[34] studied the flow behaviour and ductile damage of AA7075 aluminium alloy by developing a constitutive model coupled with the evolution of dynamic crystallization, grain size and damage. Yang et al.^[35] formulated a set of constitutive equations to investigate the underlying mechanism of flow softening and ductile damage of TA15 titanium alloy in sheet forming.

The above discussion provides an insight into the investigation of ductile fracture behaviour and damage modelling. In this study, hot tensile tests for TC6 alloy, which is a desirable material for the blade of aviation engines, were carried out to investigate the

flow behaviour, and SEM was performed on the deformed specimens to observe the fracture surface morphology and deformed microstructure. A set of constitutive equations coupling ductile damage, dislocation density, flow softening induced by adiabatic temperature rise and phase transformation, was developed, determined and verified. Afterward, the evolution of the internal variables, such as the dislocation density, adiabatic temperature rise, damage component and damage factor, was predicted and analysed.

2 Experimental details

2.1 Materials

The titanium TC6 alloy used in the present study was supplied by Baotai Group Co., Ltd. Its nominal composition is Ti-6Al-1.5Cr-2.5Mo-0.5Fe-0.3Si. The initial microstructure is shown in Fig.1. There are lath and equiaxed primary alpha phases and acicular transformed beta phase dispersed throughout the matrix. The final transformation temperature of the alpha to beta phase is 985 °C^[36].

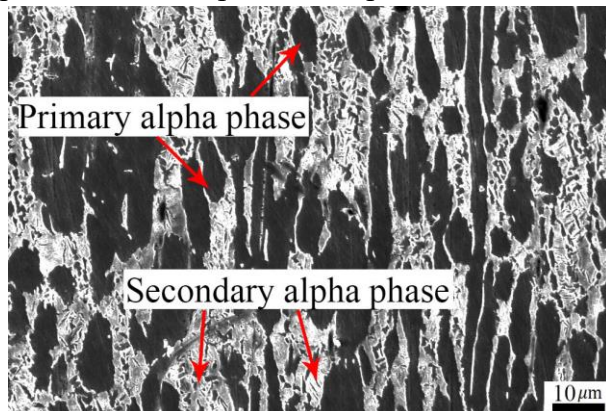
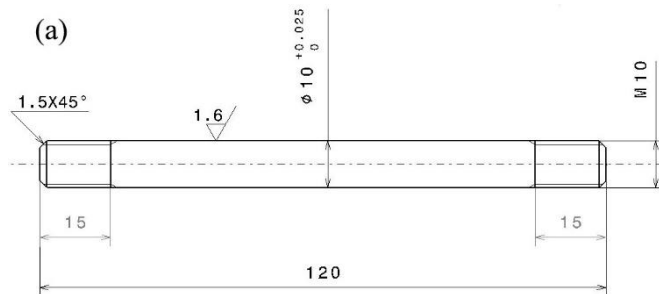
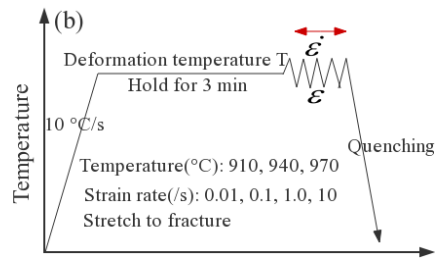


Fig. 1 Initial microstructure of the studied TC6 alloy.

2.2 Uniaxial hot tensile tests

Uniaxial hot tensile tests were conducted on a Gleeble-3500D thermal simulation machine. The specimens used in the tests were manufactured by wire-electrode cutting. Fig. 2a and Fig. 2b show the dimensions of the specimens and the experimental route, respectively. The specimens were first heated at a rate of 10 °C s⁻¹ to the predetermined temperature and held at that temperature for 3 min to obtain a balanced temperature distribution. Then, the specimens were stretched at different strain rates until fracture occurred. The deformed specimens were forced-air quenched immediately to freeze the deformed microstructure. Load-displacement curves were automatically recorded to derive the true stress-strain curves.





143

144 Fig. 2 Schematic diagrams of (a) a tensile sample and (b) the tensile test process

145 2.3 Metallographic examination

146 After cooling, the fracture surface was carefully taken from the deformed
 147 specimen and ultrasonically cleaned, and comprehensively inspected by SEM to
 148 discriminate the fracture morphology. SEM examination of the cross-section close to
 149 the fracture surface was also performed to disclose the micro damage mechanism. All
 150 the cross-sections were subjected to standard metallurgical processing and then etched
 151 with Kroll solution (HF: HNO₃: H₂O = 1: 2: 50)^[36].

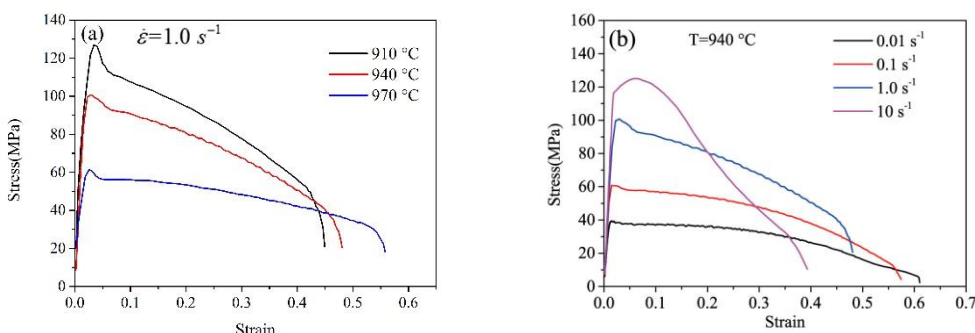
152 3 Deformation mechanisms

153 3.1 True stress-strain curves

154 Fig. 3 shows the true stress-strain curves, which were calculated from the load-
 155 displacement recorded by the hot tensile machine^[35]. It is clear that the flow stress
 156 decreases with increasing deformation temperature and decreasing strain rate. For all
 157 the flow curves, the flow stress first increases up to a peak at a small strain, defined as

158 ε_p , and the values of ε_p are less than 0.05, which indicates the tremendous
 159 accumulation of the dislocations. Soon afterwards, the flow stress decreases with the
 160 continuation of deformation due to flow softening, and when the specimens undergo
 161 necking and finally pulled off, the flow stress instantaneously drops. The strain when
 162 fracture occurs is called the failure strain ε_f . It can be seen from Fig. 3 that the values

163 of ε_f increase with increasing the deformation temperature and decreasing the strain
 164 rate, similar to the flow stress.



165

166 Fig. 3 True stress-strain curves of the studied TC6 alloy under the deformation

167 conditions of (a) $\dot{\varepsilon}=1.0\text{ s}^{-1}$ and (b) $T=940^\circ\text{C}$.

168 3.2 Flow softening mechanism

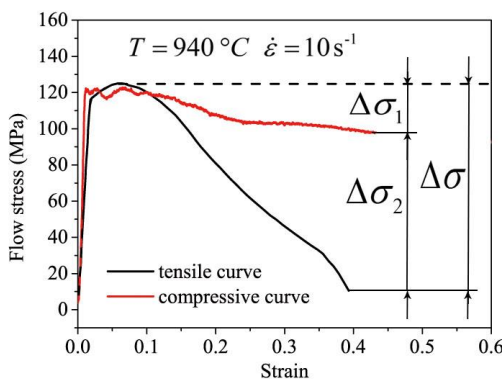
169 The accumulation of dislocations, as aforementioned, contributes to the work
170 hardening (WH) through continuous slipping and climbing, leading to a very rapid
171 increase in the flow stress. In contrast, the flow softening caused by the rearrangement
172 and annihilation of the tangled dislocations induces a reduction of the flow stress. Many
173 deformation mechanisms are attributed to the flow softening, such as dynamic recovery
174 (DRV) and DRX. For the studied TC6 alloy, no DRX was evident due to the initial
175 microstructure^[37]. However, it has been reported that adiabatic temperature rise and
176 phase transformation from the harder alpha phase to the beta phase also contribute to
177 the flow softening.

178 The flow softening caused by adiabatic temperature rise is also known as thermal
179 softening. The heat generated by the plastic deformation is trapped within the specimen
180 rather than easily dissipated, leading to an increase in the transient temperature and
181 softening of the stress response. Furthermore, the increasing temperature also lowers
182 the mobility barrier of dislocations and changes the microstructure.

183 As a two-phase titanium alloy, TC6 alloy exhibits two crystal structures, and the
184 variation of temperature enables their mutual conversion, i.e., the hexagonal close-
185 packed (*hcp*) alpha phase at lower temperature and the body-centred cubic (*bcc*) beta
186 phase at higher temperature. Because the *bcc* beta phase itself has more slip systems
187 and better crystal plasticity, the proportion of each phase affects the stress response^[19].

188 Fig. 4 shows the comparison of the hot compressive and hot tensile curves at a
189 deformation temperature of 940°C and a strain rate of 10 s^{-1} . The flow stress will be
190 restricted if the WH is counterbalanced by DRV (dashed line)^[38]. However, the flow
191 stress follows the red line if the aforementioned softening mechanism is triggered and
192 contributes to the reduction of flow stress $\Delta\sigma_1$ under compression. In the tension state,

193 the flow stress decreases $\Delta\sigma_2$ can be ascribed to the ductile damage, which reduces
194 the effective pressure bearing area as well as the applied loading. Therefore, the total
195 reduction of flow stress $\Delta\sigma$ in tensile tests can be formulated as $\Delta\sigma=\Delta\sigma_1+\Delta\sigma_2$.



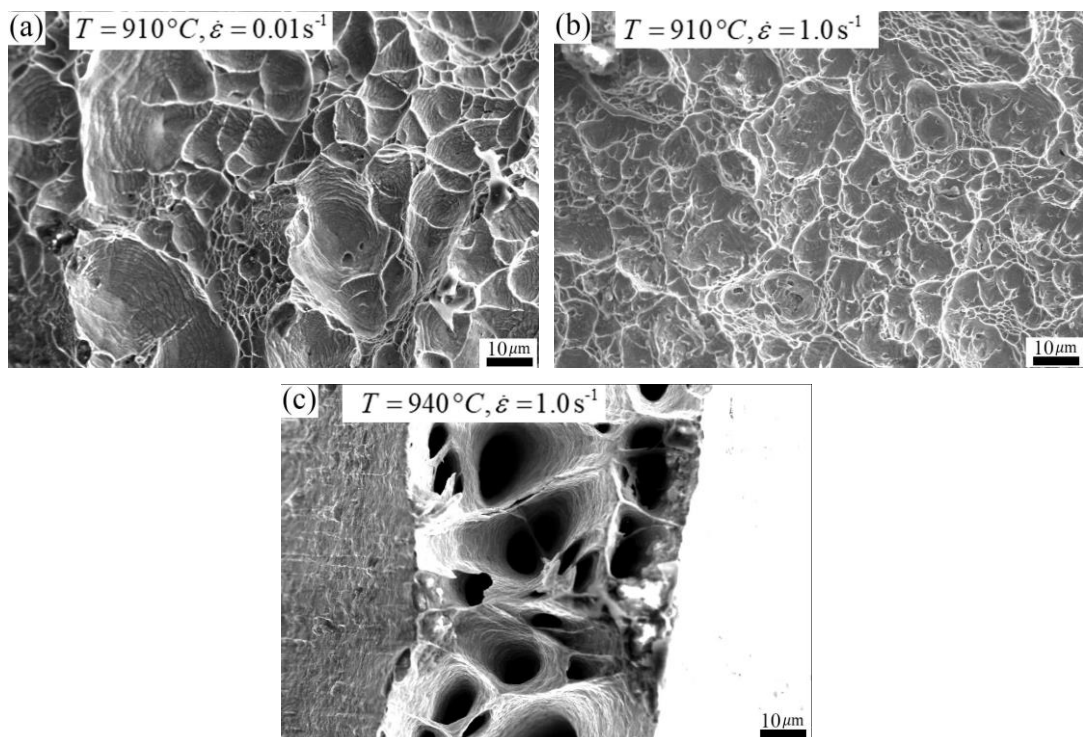
196

197 Fig. 4 Typical flow curves during hot tensile and compressive tests.

198 3.3 Fractography and damage mechanisms analysis

199 3.3.1 Fractography analysis

200 The fracture surface morphologies of the deformed specimen obtained under
201 different conditions are shown in Fig. 5. All of the fracture surfaces are fully coved by
202 dimples and voids, which are the general characteristics of ductile damage^[39]. Apart
203 from the preexisting voids, the nucleated dimples and voids grow up due to large plastic
204 deformation, and then, the dimples and voids with larger enough diameters tend to link
205 together and coalesce to form microcracks, which eventually leads to material fracture
206 or bearing failure^[40]. The nucleation and growth of the dimples and voids are
207 significantly affected by the deformation parameters. At the lower deformation
208 temperature and lower strain rate, as shown in Fig. 5a, fewer dimples and holes exist,
209 and some of these ductile dimples exhibit a larger diameter. However, the amount of
210 the ductile dimples increases with increasing the strain rate to 1.0 s^{-1} , and the ductile
211 dimples become shallower without further growth. When the deformation temperature
212 increases to $940\text{ }^{\circ}\text{C}$, the amount of the ductile dimples decreases, but the dimples grow
213 deeper. Thus, the nucleation rate of the ductile dimples increases with increasing the
214 strain rate and decreasing the deformation temperature, as does the coalescence rate of
215 the ductile dimples.



216 Fig. 5 The fracture surface morphologies of TC6 alloy under the conditions of (a)

217 $T = 910\text{ }^{\circ}\text{C}, \dot{\varepsilon} = 0.01\text{ s}^{-1}$; (b) $T = 910\text{ }^{\circ}\text{C}, \dot{\varepsilon} = 1.0\text{ s}^{-1}$; and (c) $T = 940\text{ }^{\circ}\text{C}, \dot{\varepsilon} = 1.0\text{ s}^{-1}$.

218 3.3.2 Damage mechanisms analysis

219 Fig. 6 shows the SEM images of the micro voids and cracks on the cross-section
220 located close to the fracture surface of deformed specimens. The majority of the voids
221 nucleate at the interface of the grain boundary of the equiaxed alpha phase and the

surrounding matrix, and a few initiate in the softer, ductile beta matrix. During the deformation, the microvoids are pulled and stretched to grow and link together and finally transform into microcracks. Furthermore, the coalesced cracks link the adjacent equiaxed alpha phase along the shortest path, or intersect with other cracks to form the triangular cracks. The directions of the growth, coalescence and intersection of the micro voids and cracks are in accordance with the stretching direction.

As a two-phase titanium alloy, TC6 alloy exhibits cooperative and competitive coexistence of the *hcp* alpha phase and *bcc* beta phase, as mentioned above. When the applied stress and strain concentrates at the interface of the alpha phase and beta matrix, the inconsistent strain provides a nucleation site for voids. Therefore, it can be deduced that the cavities preferentially nucleate at the interface of the alpha phase and beta matrix, and similar conclusions have been reported by Seminatin et al.^[18] and Dong et al.^[19]. Based on the microstructure examination, it is worth noting that more serrated microcracks appeared in the specimen deformed under higher temperature. The mechanisms involved have not been reported up to now, so further research is needed.

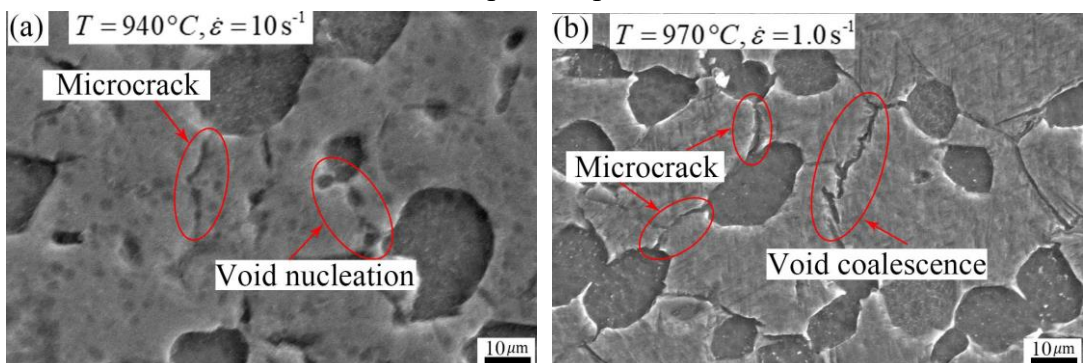


Fig. 6 SEM images of the micro voids and cracks on the deformed specimens.

4 Constitutive modelling

4.1 Damage evolution

The damage mechanism of the studied TC6 alloy involves void nucleation, growth and coalescence to form microcracks. Let D be the damage variable, which is formulated as follows^[41]:

$$D = \frac{A - \tilde{A}}{A} \quad (1)$$

where A is the total resisting area defined by the normal direction of the applied load, and \tilde{A} is the effective resisting area during the deformation. In the studied uniaxial hot tensile tests, the damage variable D can be defined as a scalar. From a mathematical point of view, D increases from 0 (corresponding to the undamaged state) to 1 (corresponding to the fracture state). However, the material is considered to fail when the value of D reaches a threshold, and the threshold is taken to be 0.7 in this study^[13, 35].

It has been reported that the damage evolution is greatly affected by the flow stress,

255 strain rate and strain and other variables during hot-working processes as
 256 $\dot{D} = f(\sigma, \dot{\varepsilon}_p, \varepsilon \dots)$. Moreover, the damage mechanism of the studied TC6 alloy is
 257 very similar to what occurs in the works of Semiatin et al.^[18], Lin et al.^[13, 42], and Yang
 258 et al.^[35]. Therefore, the damage model proposed by Lin et al.^[13] is adopted. As a handful
 259 of the voids directly nucleates in the beta matrix due to the concentration of stress and
 260 strain, so the model has been modified as follows:

$$261 \quad D = D_{nucleation} + D_{growth} \quad (2)$$

$$262 \quad \dot{D}_{nucleation} = \beta_1 (1 - D) |\dot{\varepsilon}_{p,\alpha} - \dot{\varepsilon}_{p,\beta}|^{\beta_2} \sigma^{\beta_3} \quad (3)$$

$$263 \quad \dot{D}_{growth} = \frac{\beta_4 \cosh(\beta_5 \varepsilon_p) \dot{\varepsilon}_p^{\beta_6}}{(1 - D)^{\beta_7}} \quad (4)$$

264 where $\dot{D}_{nucleation}$ and \dot{D}_{growth} represent the void nucleation and void growth rates,
 265 respectively. β_1 and β_4 are the temperature dependent parameters that control the
 266 rates of nucleation and growth from the overall perspective. β_2 and β_3 correspond
 267 to the effects of inconsistent strain and flow stress, respectively. β_5 is a temperature-
 268 dependent parameter that adjusts the growth of voids with increasing deformation strain.
 269 The temperature dependent parameter β_6 represents the effect of the applied strain
 270 rate on the growth of voids. β_7 restricts the ε_f to less than the threshold.

271 4.2 Flow softening evolution

272 Based on the aforementioned discussion, the flow softening of the studied TC6
 273 alloy can be ascribed to adiabatic temperature rise and phase transformation, which can
 274 be formulated as follows^[9, 13]:

$$275 \quad T_\varepsilon = \eta \frac{\sigma}{cd} |\dot{\varepsilon}_p| \quad (5)$$

$$276 \quad \dot{f}_\beta = \mu_l \left(\frac{f_\beta}{0.5} \right)^{\mu_2} (1 - f_\beta)^{\mu_3} T_\varepsilon \quad (6)$$

277 where T_ε represents the adiabatic temperature rise converted from the deformation
 278 energy and η is the conversion coefficient. c and d are the specific heat and material
 279 density, respectively. In Eq. (6), f_β represents the volume fraction of beta phase, μ_l ,

280 μ_2 and μ_3 are material constants determined by the phase transformation test, and the
 281 corresponding details about the test procedure and results are described elsewhere^[36].

282 4.3 Plastic flow rule

283 Generally, the overall flow stress can be divided into the initial yield stress, WH
 284 stress and viscoplastic stress:

285
$$\sigma = k + H + \sigma_v \quad (7)$$

286 where σ (MPa) is the total flow stress, k (MPa) is the initial yield stress, H
 287 (MPa) is the WH stress and σ_v (MPa) is the viscoplastic stress.

288 According to the Norton's law $\dot{\epsilon}_p = (\sigma_v / \lambda^*)^{N^*}$, the flow rule of the material can
 289 be described as Eq. (8):

290
$$\dot{\epsilon}_p = \left\langle \frac{\sigma - k - H}{K} \right\rangle^n \quad (8)$$

291 where $\dot{\epsilon}_p$ (s^{-1}) is the plastic strain rate, K is a temperature-dependent parameter, n is
 292 the viscosity exponent. $\langle \rangle$ represents the Macaulay brackets, which means that the
 293 term is inapplicable only when the plastic deformation occurs.

294 Concerning TC6 alloy, a typical two-phase titanium alloy, the plastic strain rate
 295 can be decomposed into two parts, the plastic strain rates of the alpha and beta phases,
 296 as shown below^[9, 35]:

297
$$\dot{\epsilon}_p = \dot{\epsilon}_{p,\alpha}(1-f_\beta) + \dot{\epsilon}_{p,\beta}f_\beta \quad (9)$$

298 where $\dot{\epsilon}_{p,\alpha}$ and $\dot{\epsilon}_{p,\beta}$ are the plastic strain rates of the alpha and beta phases,
 299 respectively. During the hot tensile deformation, the side effect of ductile damage on
 300 the total flow stress needs to be considered. Then, the flow rule is rewritten as follows:

301
$$\dot{\epsilon}_{p,\alpha} = \left\langle \frac{\sigma/(1-D) - k_\alpha - H}{K_\alpha} \right\rangle^n \quad (10)$$

302
$$\dot{\epsilon}_{p,\beta} = \left\langle \frac{\sigma/(1-D) - k_\beta - H}{K_\beta} \right\rangle^n \quad (11)$$

303 where k_α and k_β are the initial yield stresses of the alpha and beta phases,
 304 respectively, and they are temperature dependent and decrease with increasing
 305 temperature. K_α and K_β are also temperature-dependent parameters that decrease

306 with increasing temperature.

307 According to Hooke's law, the total flow stress of a material under hot tensile
308 deformation is calculated by^[34]:

309 $\sigma = (1-D)E(\varepsilon_T - \varepsilon_p)$ (12)

310 where ε_T denotes the total strain, and E represents the intrinsic Young's modulus of
311 the material, which is a temperature-dependent parameter that decreases with
312 increasing temperature.

313 4.4 Dislocation density evolution

314 Under the hot tensile conditions, the material is subjected to high temperature and
315 plastic deformation accompanied by the evolution of the dislocation density. Various
316 deformation mechanisms are involved. The generation of the new dislocation and their
317 climbing with the existing dislocations causes the multiplication of dislocations and
318 working hardening. Meanwhile, the stored energy of the material enhances and drives
319 the recovery and microstructure change. Conversely, the recovery, including the statics
320 and dynamics recovery, leads to absorption of the tangled dislocations, causing the
321 annihilation of dislocation. Bai et al.^[9] and Yang et al.^[35] formulated the evolution of the
322 dislocation density as Eq. (13). To adjust for the effect of the plastic strain rate, a
323 controlled coefficient δ_l was introduced, as Eq. (14) shows:

324 $\dot{\bar{\rho}} = A(1-\bar{\rho})|\dot{\varepsilon}_p| - C\bar{\rho}^\delta$ (13)

325 $\dot{\bar{\rho}} = A(1-\bar{\rho})|\dot{\varepsilon}_p|^{\delta_l} - C\bar{\rho}^\delta$ (14)

326 where $\dot{\bar{\rho}}$ is the evolution rate of normalized dislocation density. And A and C are
327 temperature-dependent parameters that decrease with decreasing temperature. δ is
328 material parameter that controls the effect of static recovery.

329 The isotropic WH is closely related to the accumulation and annihilation of
330 dislocations, therefore, it is formulated as shown below^[33]:

331 $H = B\bar{\rho}^{0.5}$ (15)

332 where $\bar{\rho}$ is the normalized dislocation density. B is a temperature-dependent
333 parameter that decreases with increasing temperature.

334 The aforementioned temperature-dependent parameters are summarized in Table
335 1, and all of them are formulated in Arrhenius relations based on their variation
336 tendency with the deformation temperature. In Table 1, R is the universal gas constant
337 which equals to $8.3145 \text{ J} \cdot \text{mol}^{-1} \cdot \text{K}^{-1}$, and T is the absolute temperature in K .

338
339 Table 1 List of temperature dependent parameters.

$k_\alpha = k_{\alpha,0} \exp(Q_k / RT)$	$K_\alpha = K_{\alpha,0} \exp(Q_K / RT)$	$n = n_0 \exp(Q_n / RT)$
$E = E_0 \exp(Q_E / RT)$	$B = B_0 \exp(Q_B / RT)$	$A = A_0 \exp(-Q_A / RT)$
$C = C_0 \exp(-Q_C / RT)$	$\beta_1 = \beta_{1,0} \exp(Q_1 / RT)$	$\beta_4 = \beta_{4,0} \exp(Q_4 / RT)$
$\beta_5 = \beta_{5,0} \exp(Q_5 / RT)$	$\beta_6 = \beta_{6,0} \exp(Q_6 / RT)$	$\beta_7 = \beta_{7,0} \exp(Q_7 / RT)$

340 5 Results and discussions

341 5.1 Determination of material constants

342 Two steps are required to determine the material constants. However, the phase
 343 transformation process is identical to that in the test that has already been carried out
 344 by the author due to the consistency of the experimental material^[36]. Therefore, the
 345 material constants μ_1 , μ_2 and μ_3 were employed in the present study. The next step
 346 is to determine the rest of the parameters based on the experimental stress-strain flow
 347 curves. An optimization method based on a genetic algorithm (GA) in MATLAB
 348 software was adopted by minimizing the residuals between the experimental and
 349 computed values. The details of the optimization process have been described by
 350 elsewhere^[42]. The determined material constants are listed in Table 2.

351 Table 2 Determined values of material constants

Material constants	Optimal value	Material constants	Optimal value
$k_{\alpha,0}$ (MPa)	9.7803E-4	$Q_k (J \bullet mol^{-1})$	9.1160E4
$K_{\alpha,0}$ (MPa)	8.2681E-2	$Q_K (J \bullet mol^{-1})$	6.5647E4
E_0 (-)	4.0811E3	$Q_E (J \bullet mol^{-1})$	5.0858E3
B_0 (MPa)	1.0173E0	$Q_B (J \bullet mol^{-1})$	4.2972E4
A_0 (-)	6.8775E2	$Q_A (J \bullet mol^{-1})$	5.1523E4
C_0 (-)	2.7851E17	$Q_C (J \bullet mol^{-1})$	3.4876E5
$\beta_{1,0}$ (-)	2.0196E-3	$Q_{\beta_1} (J \bullet mol^{-1})$	7.0475E4
$\beta_{4,0}$ (-)	1.348E-2	$Q_{\beta_4} (J \bullet mol^{-1})$	4.6921E4
$\beta_{5,0}$ (-)	1.2870E-1	$Q_{\beta_5} (J \bullet mol^{-1})$	3.4987E4
$\beta_{6,0}$ (-)	4.1143E-1	$Q_{\beta_6} (J \bullet mol^{-1})$	3.4948E4

$\beta_{7,0}^{(-)}$	2.5203E-2	$Q_{\beta_7}(J \bullet mol^{-1})$	1.3485E4
$\delta^{(-)}$	1.1265	$\delta_1^{(-)}$	4.6923
$\eta^{(-)}$	0.9558	$\beta_2^{(-)}$	1.5598
$\beta_3^{(-)}$	5.0182		

352 5.2 Validation of the constitutive equations

353 Fig. 7 shows the comparison of the flow stress between the experimental (symbol)
 354 and computed (line) results under different deformation temperatures. The deformation
 355 mechanisms, including WH, flow softening and ductile damage, can be satisfactorily
 356 predicted. Most of the experimental values are close to the computed line, which
 357 indicates a good prediction of the developed constitutive model.

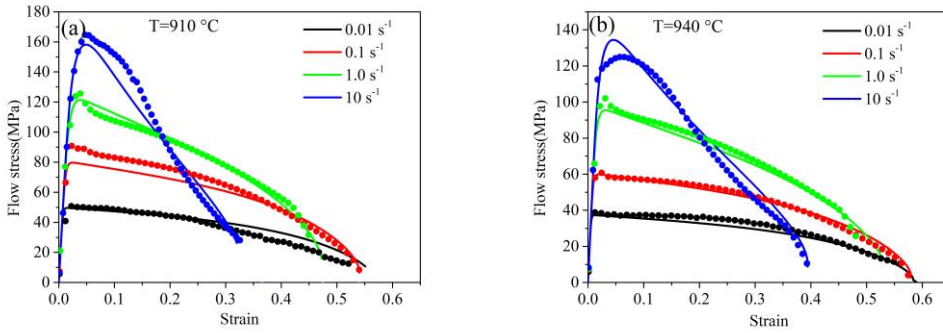
358 To evaluate the degree of linear correlation of the proposed constitutive equations,
 359 some indexes for statistical analysis, including the correlation coefficient (R), the
 360 average absolute relative error ($AARE$) and the root mean square error ($RMSE$), were
 361 calculated as:

$$362 \quad R = \frac{\sum_{i=1}^N (E_i - \bar{E})(P_i - \bar{P})}{\sqrt{\sum_{i=1}^N (E_i - \bar{E})^2 \sum_{i=1}^N (P_i - \bar{P})^2}} \quad (16)$$

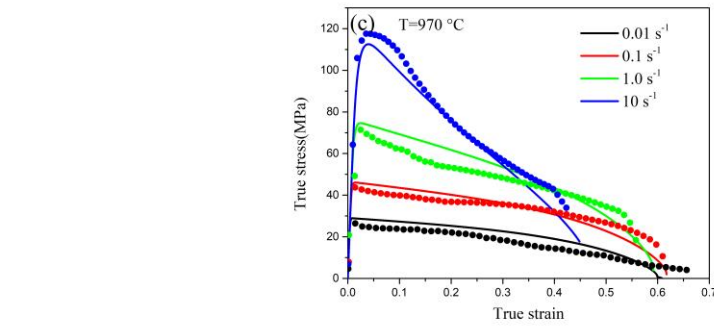
$$363 \quad AARE = \frac{1}{N} \sum_{i=1}^N \left| \frac{E_i - P_i}{E_i} \right| \times 100\% \quad (17)$$

$$364 \quad RMSE = \sqrt{\frac{1}{N} \sum_{i=1}^N (E_i - P_i)^2} \quad (18)$$

365 where E_i and \bar{E} are the experimental stress and average experimental stress,
 366 respectively. P_i and \bar{P} are the computed stress and average computed stress
 367 predicted by the developed constitutive model, respectively. N is the total number of
 368 the calculated points. Fig. 8 shows the best linear fitting between the experimental and
 369 computed stresses at different deformation temperatures and strain rates. It can be seen
 370 that the R is very close to 1.0, and the maximum values of $AARE$ and $RMSE$ are 5.4986%
 371 and 3.1572%, respectively, which manifests the developed model has a good
 372 forecasting capability.



373

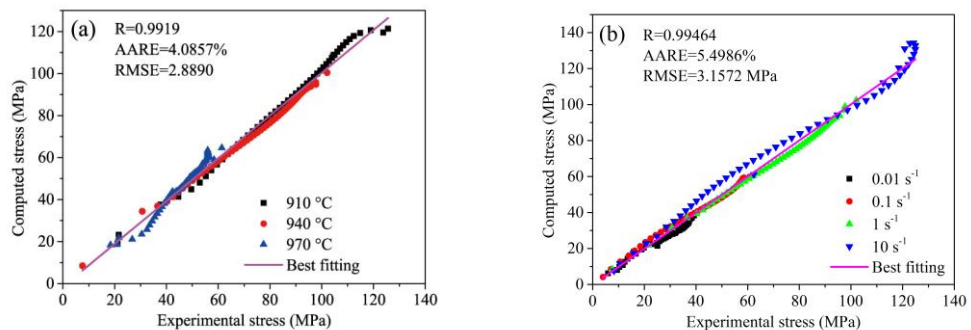


374

375 Fig.7 Comparison of the experimental (symbol) and computed (line) stress data at
376 different deformation temperatures of (a) $T=910^{\circ}\text{C}$, (b) $T=940^{\circ}\text{C}$ and (c)
 $T=970^{\circ}\text{C}$.

377

$T=970^{\circ}\text{C}$.



378

379 Fig. 8 Correlation between the experimental and computed stresses at different
380 deformation conditions of (a) $\dot{\varepsilon}=1.0\text{s}^{-1}$ and (b) $T=940^{\circ}\text{C}$.

381 5.3 Evolution of the internal variables

382 Fig. 9a shows the evolution of the computed normalized dislocation density. The
383 competing processes involved in the evolution of dislocations are accurately predicted.
384 The dislocation density increase sharply in the initial stage of deformation due to the
385 creation and accumulation of dislocations, which causes the WH. Then, it remains

stable immediately following a peak, which is attributed to the rearrangement and annihilation of dislocations by the static and dynamic recovery. Overall, the normalized dislocation density increases with decreasing deformation temperature and increasing strain rate.

The evolution of the adiabatic temperature rise under different deformation temperatures and strain rates was shown in Fig. 9b. According to Eq. (10), the adiabatic temperature rise is a function of the flow stress, plastic strain, specific heat capacity and mass density. Therefore, it increases with increasing strain at a given deformation temperature and strain rate. An increase in temperature has a negative effect on changes in the adiabatic temperature rise, but an increase in strain rate exhibits the opposite trend. When the specimen is deformed under the lowest strain rate of 0.01 s^{-1} , the adiabatic temperature rise is very small. These results support the conclusion proposed by Khan et al.^[43] that the adiabatic temperature rise has a more significant influence on the specimens deformed under a higher strain rate. Therefore, instead of the adiabatic temperature rise, other softening mechanisms, such as dynamic/statics recovery and phase transformation, are the main reasons for the flow softening when the strain rate is very low.

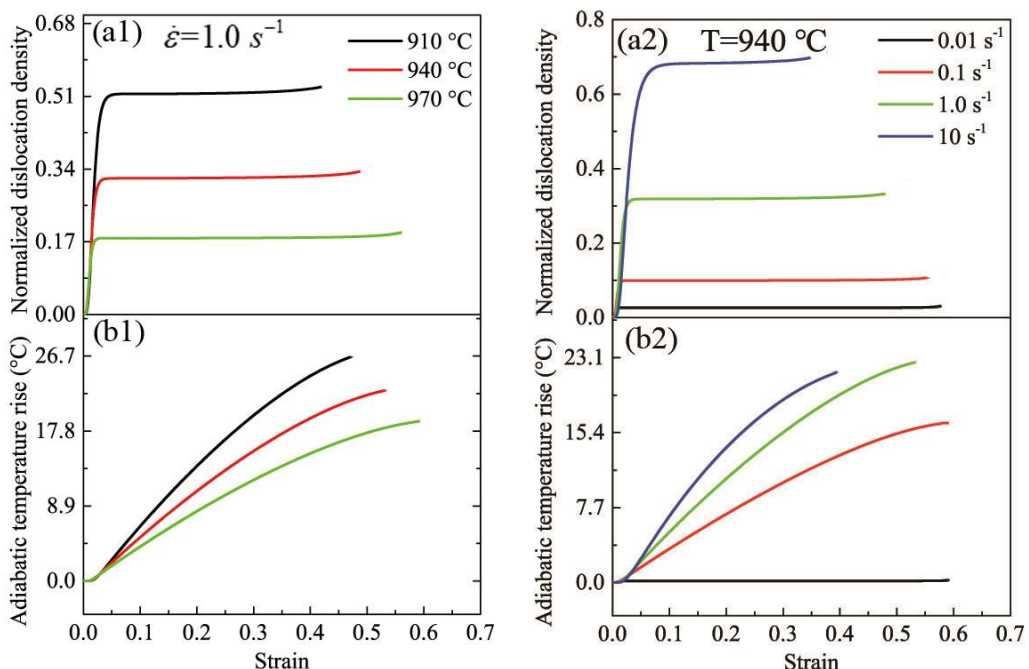
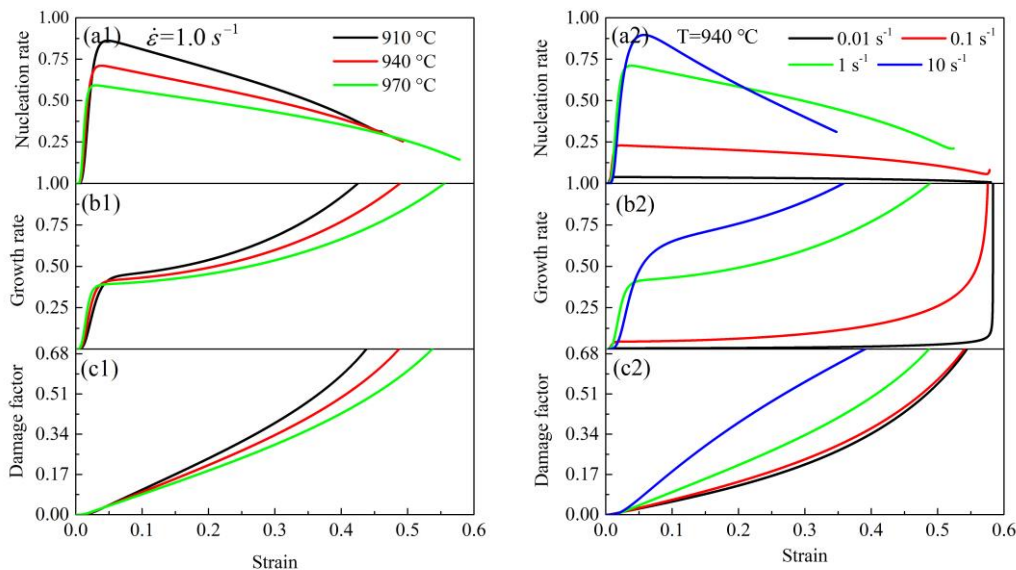


Fig. 9 Predicted evolution of the (a) Normalized dislocation density and (b) adiabatic temperature rise under different deformation temperatures and strain rates.

The ductile damage mechanism of the studied TC6 alloy, under a uniaxial tensile test, is assumed to be the nucleation and growth of micro defects. Notwithstanding, dynamically tracking the relationship between the nucleation and growth of microdefects and stretching strain using precision density measurements or quantitative metallography during the tests is difficult, this relationship can be predicted by the developed constitutive model. Fig. 10 shows the damage components, including nucleation rate and growth rate, and damage factor as a function of the true strain under

413 different conditions. Clearly, the nucleation and growth rates increase with decreasing
 414 deformation temperature and increasing strain rate, which is consistent with the
 415 fractography observations. Under a higher strain rate of 1.0 s^{-1} , the nucleation rate
 416 increases sharply with strain and then decreases relatively slowly (Fig. 10a1). In
 417 contrast, the growth rate achieves a significant rise at a larger strain (Fig. 10b1). This
 418 result indicates that the microdefects mainly nucleate in the early stage of deformation,
 419 but primarily grow and link together with continuing deformation. The nucleation and
 420 growth rates for each strain rate under a deformation temperature of $940 \text{ }^\circ\text{C}$ vary widely,
 421 especially at a lower strain rate of 0.01 s^{-1} . Fig. 10c shows the evolution of the computed
 422 total damage factor. Similarly, the damage factor increases with decreasing deformation
 423 temperature and increasing strain rate. The damage factor increases linearly from 0 at
 424 the initial deformation, which indicates that the material is undamaged. Then, the
 425 damage factor exhibits a rapidly increase due to the accumulation of microdefects until
 426 the materials fails.



427

428 Fig. 10 Prediction of the (a) nucleation rate, (b) growth rate and (c) damage factor
 429 under different deformation temperatures and strain rates.

430 6 Conclusion

- 431 (1) The flow softening and ductile damage behaviours of TC6 alloy were investigated
 432 under uniaxial hot tensile conditions. The flow stress rapidly increases to a peak at
 433 a tiny strain, followed by a decrease in stress due to flow softening and ductile
 434 damage.
- 435 (2) SEM observations reveal that the ductile damage of the studied TC6 alloy can be
 436 ascribed to the nucleation and growth of microdefects. The microvoids
 437 preferentially nucleate at the interface of the alpha phase and beta matrix due to the
 438 inconsistent strain between the *hcp* alpha phase and *bcc* beta phase.
- 439 (3) A set of unified viscoplastic constitutive equations including flow softening and
 440 ductile damage mechanisms has been developed, determined and verified. The

441 computed flow stress agrees well with the experimental data, and the maximum
442 values of *AARE* and *RMSE* are 5.4986% and 3.1572%, respectively, which indicates
443 the reliability of the prediction of the developed model.

444 (4) The predicted normalized dislocation density increases with decreasing
445 deformation temperature and increasing strain rate. The adiabatic temperature rise
446 has a more significant influence when the specimen is deformed under higher strain
447 rates. The predicted damage components show that the microdefects mainly
448 nucleate in the early stage of deformation but then primarily grow and link together
449 with continuing deformation.

450

451 Acknowledgment

452 This work was supported by the National Natural Science Foundation of China
453 [Grant No. 51505026], and was also supported by the Beijing Laboratory of Modern
454 Transportation Metal Materials and Processing Technology.

455 Reference

- 456 [1]. C. Leyens, M. Peters, Titanium and titanium alloys: Fundamentals and
457 Applications, 1st ed., betz-druck GmbH, Darmstadt, 2003.
- 458 [2]. A. Momeni, S.M. Abbasi, Effect of hot working on flow behavior of Ti–6Al–4V
459 alloy in single phase, *Mater. Des.* 31 (2010) 3599–3604.
- 460 [3]. X.G. Fan, H. Yang, P.F. Gao, Prediction of constitutive behavior and
461 microstructure evolution in hot deformation of TA15 titanium alloy, *Mater. Des.* 51
462 (2013) 34–42.
- 463 [4]. H.Q. Liang, H.Z. Guo, Y. Nan, C. Qin, X.N. Peng, J.L. Zhang, The construction of
464 constitutive model and identification of dynamic softening mechanism of high-
465 temperature deformation, *Mater. Sci. Eng. A* 615 (2014) 42–50.
- 466 [5]. F.S. Qu, Y.H. Zhou, L.Y. Zhang, Z.H. Wang, J. Zhou, Research on hot deformation
467 behavior of Ti–5Al–5Mo–5V–1Cr–1Fe alloy, *Mater. Des.* 69 (2015) 153–162.
- 468 [6]. J. Luo, M.Q. Li, X.L. Li, Y.P. Shi, Constitutive model for high temperature
469 deformation of titanium alloys using internal state variables, *Mech. Mater.* 42 (2010)
470 157–165.
- 471 [7]. C. Li, X.Y. Zhang, K.C. Zhou, C.Q. Peng, Relationship between lamellar a
472 evolution and flow behavior during isothermal deformation of Ti-5Al-5Mo-1Cr-1Fe
473 near β titanium alloy, *Mater. Sci. Eng. A* 558 (2012) 668–674.
- 474 [8]. Y.Q. Ning, B.C. Xie, H.Q. Liang, H. Li, X.M. Yang, H.Z. Guo, Dynamic softening
475 behavior of TC18 titanium alloy during hot, *Mater. Des.* 71 (2015) 68–77.
- 476 [9]. Q. Bai, J. Lin, T.A. Dean, D.S. Balint, T. Gao, Z. Zhang, Modelling of dominant
477 softening mechanisms for Ti-6Al-4V, *Mater. Sci. Eng. A* 559 (2013) 352–358.
- 478 [10]. L.J. Huang, L. Geng, A.B. Li, X.P. Cui, H.Z. Li, G.S. Wang, Characteristics of hot
479 compression behavior of Ti–6.5Al–3.5Mo–1.5Zr–0.3Si alloy with an equiaxed
480 microstructure, *Mater. Sci. Eng. A* 505 (2009) 136–143.
- 481 [11]. J. Guo, L.F. Wang, S.F. Liu, M.Q. Li, The correlation between the flow behavior
482 and the microstructure evolution during hot working of TC18 alloy, *Mater. Sci. Eng. A*

- 483 654 (2016) 213-220.
- 484 [12]. P.F. Gao, M. Zhen, X.G. Fan, Z.N. Lei, Y. Cai, Hot deformation behavior and
485 microstructure evolution of TA15 titanium alloy with nonuniform microstructure,
486 *Mater. Sci. Eng. A* 654 (2016) 213-220.
- 487 [13]. J. Lin, Y. Liu, T.A. Dean, A Review on damage mechanisms, models and
488 calibration methods under various deformation conditions, *Int. J. Damage. Mech.* 14
489 (2005) 299-319.
- 490 [14]. R. Bobbili, V. Madhu, Flow and fracture characteristics of near alpha titanium
491 alloy, *J. Alloy. Compd.* 684 (2016) 162-170.
- 492 [15]. M.S. Mohamed, A.D. Foster, J.G. Lin, D.S. Balint, T.A. Dean, Investigation of
493 deformation and failure features in hot stamping of AA6082: Experimentation and
494 modelling, *Int. J. Mech. Tool. Manuf.* 53 (2012) 27-38.
- 495 [16]. M.A. Khaleel, H.M. Zbib, E.A. Nyberg, Constitutive modeling of deformation
496 and damage in superplastic materials, *Int. J. Plasticity.* 17 (2001) 277-296.
- 497 [17]. S.L. Semiatin, R.L. Goetz, E.B. Shell, V. Seetharaman, A.K. Ghosh, Cavitation
498 and failure during hot forging of Ti-6Al-4V, *Metall. Mater. Trans. A* 30A (1998) 1411-
499 1424.
- 500 [18]. S.L. Semiatin, V. Seetharaman, E.B. Shell, M.P. Simon, P.N. Fagin, Cavitation
501 during hot tension testing of Ti-6Al-4V, *Mater. Sci. Eng. A* 256 (1998) 92-110.
- 502 [19]. X.J. Dong, S.Q. Lu, H. Z. Zheng, X. Li, D.L. Ouyang, Cavity nucleation during
503 hot forging of Ti-6Al-2Zr-1Mo-1V alloy with colony alpha microstructure, *Trans.*
504 *Nonferrous. Met. Soc. China.* 20 (2010) 2259-2264.
- 505 [20]. P.D. Nicolaou, R.L. Goetz, S.L. Semiatin, Influence of stress state on cavitation
506 during hot working of Ti-6Al-4V, *Metall. Mater. Trans. A* 35A (654-662).
- 507 [21]. R. Bobbili, V. Madhu, Effect of strain rate and stress triaxiality on tensile behavior
508 of titanium alloy Ti-10-2-3 at elevated temperatures, *Mater. Sci. Eng. A* 667 (2016) 33-
509 41.
- 510 [22]. M.G. Cockcroft, D.J. Latham, Ductility and the workability of metals, *Journal of*
511 *the Institute of Metals.* 96 (1968) 33-39.
- 512 [23]. D.Y. Seok, D. Kim, S.W. Kim, J. Bak, Y.S. Lee, K. Chung, Fracture criterion for
513 AZ31 Mg alloy plate at elevated temperature, *Met. Mater. Int.* 21 (2015) 54-71.
- 514 [24]. G.R. Johnson, W.H. Cook, Fracture characteristics of three metals subjected to
515 various strains, strain rates, temperature and pressures, *Eng. Fract. Mech.* 21 (1985) 31-
516 48.
- 517 [25]. F.A. Mcclintock, A criterion for ductile fracture by the growth of holes, *J. Appl.*
518 *Mech.* 35 (1968) 363-371.
- 519 [26]. M. Oyane, Criteria of ductile fracture strain, *Jsme. Int, J.* 15 (1972) 1507-1513.
- 520 [27]. J.R. Rice, D.M. Rracey, On the ductile enlargement of voids in triaxial stress fields,
521 *J. Mech. Phys. Solids.* 17 (1969) 201-217.
- 522 [28]. A.L. Gurson, Continuum theory of ductile rupture by void nucleation and growth:
523 Part I-yield criteria and flow rules for porous ductile media, *J. Eng. Mater.* 1 (1977)
524 2-15.
- 525 [29]. V. Tvergaard, A. Needleman, Analysis of the cup-cone fracture in a round tensile
526 bar, *Acta Metall.* 32 (1984) 157-169.

- 527 [30]. V. Tvergaard, On localization in ductile materials containing spherical voids, *Int.*
528 *J. Fracture*. 18 (1982) 237-252.
- 529 [31]. D.R. Hayhurst, M.T. Wong, F. Vakilizahami. The use of CDM analysis techniques
530 in high temperature creep failure of welded structures, *Int. J. A-Solid. M.* 45 (2001) 90-
531 97.
- 532 [32]. J. Lin, M Mohamed, D. Balint and T.A. Dean. The development of continuum
533 damage mechanics-based theories for predicting forming limit diagrams for hot
534 stamping applications, *Int. J. Damage. Mech.* 23 (2014) 684-701.
- 535 [33]. Y.M. Huo, J.G. Lin, Q. Bai, B.Y. Wang, X.F. Tang, H.C. Ji, Prediction of
536 microstructure and ductile damage of a high-speed railway axle steel during cross
537 wedge rolling, *J. Mater. Process. Tech.* 239 (2017) 359-369.
- 538 [34]. W.C. Xiao, B.Y. Wang, Y. Wu, X.M. Yang, Constitutive modeling of flow behavior
539 and microstructure evolution of AA7075 in hot tensile deformation, *Mater. Sci. Eng. A*
540 721 (2018) 704-713.
- 541 [35]. L. Yang, B.Y. Wang, G. Liu, H.J. Zhao, W.C. Xiao, Behavior and modeling of
542 flow softening and ductile damage evolution in hot forming of TA15 alloy sheets, *Mater.*
543 *Des.* 85 (2015) 135-148.
- 544 [36]. J.L. Li, B.Y. Wang, H. Huang, S. Fang, P. Chen, J.X. Shen, Unified modelling of
545 the flow behaviour and softening mechanism of aTC6 titanium alloy during hot
546 deformation, *J. Alloy. Compd.* 748 (2018) 1031-1043.
- 547 [37]. G.Z. Quan, D.S. Wu, G.C. Luo, Y.F. Xia, J. Zhou, Q. Liu, L. Gao, Dynamic
548 recrystallization kinetics in α phase of as-cast Ti-6Al-2Zr-1Mo-1V alloy during
549 compression at different temperatures and strain rates, *Mater. Sci. Eng. A* 589 (2014)
550 23-33.
- 551 [38]. G.Z. Quan, G.C. Luo, J.T. Liang, D.S. Wu, A. Mao, Q. Liu, Modelling for the
552 dynamic recrystallization evolution of Ti-6Al-4V alloy in two-phase temperature range
553 and a wide strain rate range, *Comp. Mater. Sci.* 97 (2015) 136-147.
- 554 [39]. W. Garrison. Ductile fracture. *J. Phys. Chem. Solids.* 48 (1987) 1035-1074.
- 555 [40]. J. Besson, Continuum models of ductile fracture: A review, *Int. J. Damage. Mech.*
556 19 (2010) 3-52.
- 557 [41]. J. Lemaitre, A continuous damage mechanics model for ductile fracture, *J. Eng.*
558 *Mater-T. Asme.* 107 (1985) 83-89.
- 559 [42]. J. Lin, B.H. Cheong, X. Yao, Universal multi-objective function for optimising
560 superplastic-damage constitutive equations, *J. Mater. Process. Tech.* 125 (2002) 199-
561 205.
- 562 [43]. A.S. Khan, R. Kazmi, B. Farrokh, M. Zupan, Effect of oxygen content and
563 microstructure on the thermos-mechanical response of three Ti-6Al-4V alloys:
564 Experimental and modeling over a wide range of strain-rates and temperatures, *Int. J.*
565 *Plasticity.* 23 (2007) 1105-1125.